

# Molecular Electronic Study of Spiro-[cyclopenta[1,2-*b*:5,4-*b'*]dithiophene-4,9'-fluorene] Derivatives: Route to Decent Hole-Transporting Materials

Zilong Zhang, Wenbo Li, Simonetta Orlandi,\* Marco Cavazzini, Abdullah M. Asiri, Mohammad Khaja Nazeeruddin, Gianluca Pozzi, Michael Saliba,\* and Peng Gao\*

Cite This: *J. Phys. Chem. C* 2022, 126, 18238–18250

Read Online

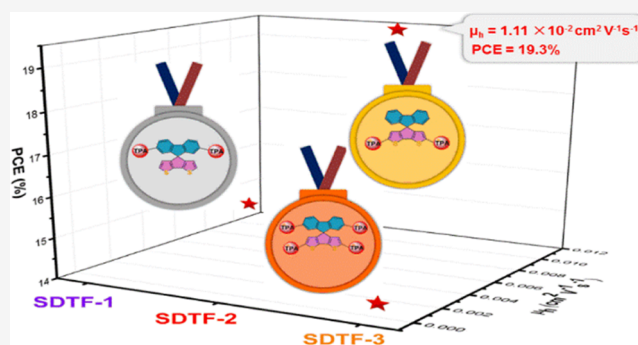
ACCESS |

Metrics & More

Article Recommendations

Supporting Information

**ABSTRACT:** Spiro-type molecules have been extensively explored as hole-transporting materials (HTMs) in perovskite solar cells (PSCs). However, a closer look at the rule of design of such molecules is missing, and a combined experimental and theoretical study is needed. In this work, three spiro-[cyclopenta[1,2-*b*:5,4-*b'*]dithiophene-4,9'-fluorene] (SDTF) derivatives decorated with triphenylamine have been designed and synthesized. The thermal and optoelectronic properties, single-crystal structures, and charge-transport properties have been extensively investigated to reveal the impact of the linkage position of triphenylamine groups by combining experimental and theoretical methods, and the results are consistent with each other. Moreover, transfer integrals and reorganization energies in these molecules are also calculated to predict hole mobility. Our comprehensive studies show that SDTF-2 with a suitable energy alignment, good hole injection/transportability, and high theoretical hole mobility can be employed for efficient perovskite solar cells, achieving a high power conversion efficiency of 19.3%. In addition, first-principle calculations reveal that the strong interactions between SDTF-2 and the perovskite surface can facilitate fast hole extraction. Our way of study has provided useful information as part of the Materials Genome Initiative. We hope our investigation will offer a reliable path to predict or find the potential of novel spiro-type HTMs to become the alternative choice of spiro-OMeTAD.



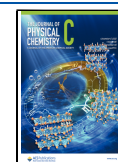
## 1. INTRODUCTION

Spiro-type organic semiconductors with a core of 9,9'-spirobifluorene represented by 2,2',7,7'-tetrakis(*N,N*-di-*p*-methoxyphenylamine)-9,9'-spirobifluorene (spiro-OMeTAD) have been intensively studied as promising hole-transporting materials (HTMs) in conventional *n-i-p*-type perovskite solar cell (PSC) devices.<sup>1–17</sup> The structure of such molecules comprises two identical or different  $\pi$ -conjugated systems connected by a common  $\text{sp}^3$ -hybridized carbon atom, resulting in different solubility, glass transition temperature, and mechanical stability.<sup>18,19</sup>

So far, albeit the popularity of the spiro-OMeTAD,<sup>20,21</sup> its stability, complicated synthetic procedures, expensive purification cost, and low intrinsic hole mobility have limited its application in commercialized PSC modules. Therefore, much effort has been devoted to developing more economical and efficient alternatives to spiro-OMeTAD,<sup>22–25</sup> and the same spiro cores were connected to heterocycles such as thiophene and pyrane rings.<sup>3,26–28</sup> Among them, spiro-[cyclopenta[1,2-*b*:5,4-*b'*]dithiophene-4,9'-fluorene] (SDTF) core derivatives deserve particular attention because of their ease of tunability by molecular engineering and peculiar optoelectronic proper-

ties. Several works have been devoted to developing SDTF core derivatives as HTMs for PSCs, and it has been demonstrated that SDTF-based molecules have the potential to become a good alternative or possibly replace spiro-OMeTAD. For example, our group reported a novel spiro-[cyclopenta[1,2-*b*:5,4-*b'*]dithiophene-4,9'-fluorene] (SDTF)-based HTM (FDT) with power conversion efficiency (PCE) exceeding 20%.<sup>27</sup> Simulations and X-ray diffraction (XRD) indicated that the molecular core had a favorable interaction with the perovskite underlayer. Recently, Schmalz et al. synthesized a series of new HTMs with an SDTF core that assisted the energy-level alignment and increased the hole mobility of the corresponding HTMs.<sup>26</sup> Despite potentially being a building block, the SDTF-based HTMs are not often

Received: August 29, 2022  
Revised: October 8, 2022  
Published: October 21, 2022



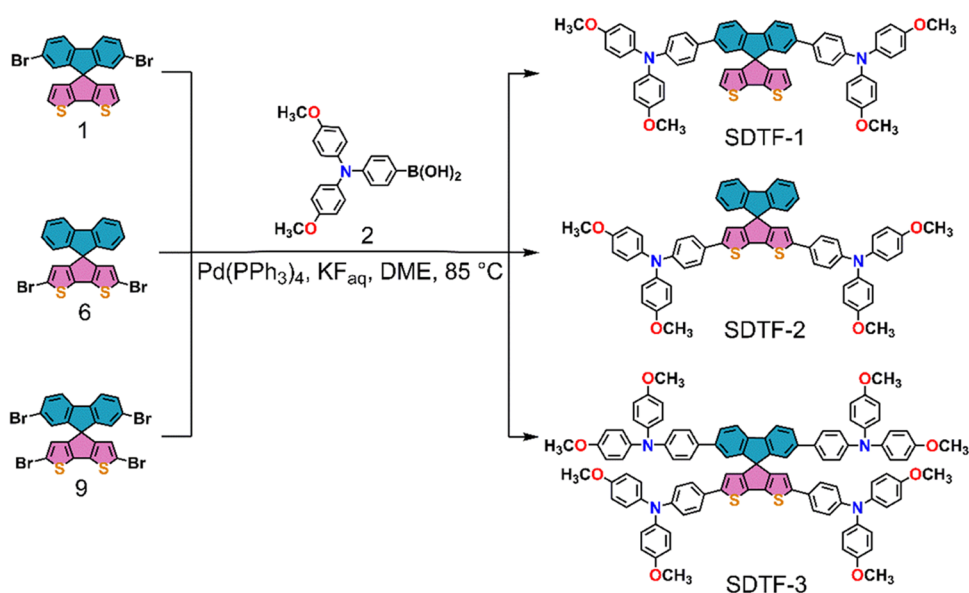


**Figure 1.** Synthetic routes and chemical structures of SDTF-1, SDTF-2, and SDTF-3.

investigated as a fundamental structure and basic unit in the literature. So far, there has been no report on the rule of design of SDTF-based molecules involving a combination of experimental and theoretical studies, and the unexploited properties of SDTF core in constructing HTMs need to be unveiled.

In this work, three SDTF derivatives were designed and synthesized by varying the linking position and number of triphenylamine (TPA) groups on the SDTF core (SDTF-1, SDTF-2, and SDTF-3, shown in Figure 1). Their solid structures were analyzed based on single crystallography and theoretical calculation, from which the effect of different configurations on the hole-transport property, intermolecular noncovalent interactions, molecular packing style, and hole mobility were extensively investigated by quantum chemical calculations. In addition to the different thermal, optical, and electrochemical properties, the three molecules exhibited distinct electronic structures, including energy level, exciton binding energy, and ionization potential. According to the computational study, SDTF-2, where the TPA units are only substituted on the cyclopentadithiophene plane, shows the best energy alignment, the highest theoretical hole mobility, and the strongest interaction with perovskite surface among the three derivatives. Therefore, the device based on SDTF-2 afforded the highest PCE of 19.3% among the three compounds (14.6% for SDTF-1 and 14.2% for SDTF-3). This work aims to establish a practical strategy to better predict the performance of SDTF-based HTMs and can offer a reliable path to construct new SDTF-based HTMs with different end-capped functional groups in the future. We hope this way of study can provide helpful guidelines for the Materials Genome Initiative.

## 2. EXPERIMENTAL SECTION

**2.1. Materials and Synthesis.** All available chemicals were purchased from commercial sources and used without any further purification. Solvents were purified by standard methods and dried if necessary. 2',7'-Dibromospiro[cyclopenta[2,1-*b*:3,4-*b'*]dithiophene-4,9'-fluorene] (1),<sup>27</sup> 4-(bis(4-methoxyphenyl)amino)phenylboronic acid (2),<sup>29</sup> 3-

bromo-5,5'-bis(trimethylsilyl)-2,2'-bithiophene (3),<sup>30</sup> and 9-(5,5'-bis(trimethylsilyl)-2,2'-bithiophen-3-yl)-2,7-dibromo-fluorene-9-ol (7)<sup>27</sup> were prepared as described in the literature. Reactions were monitored by thin layer chromatography (TLC), which was conducted on plates precoated with silica gel Si 60-F254 (Merck, Germany). Column chromatography was conducted using silica gel Si 60, 0.063–0.200 mm (normal) or 0.040–0.063 mm (flash) (Merck, Darmstadt, Germany). The preparation details of SDTF-1, SDTF-2, and SDTF-3 are described in the Supporting Information.

**2.2. Theoretical Calculations.** The ground-state and cationic geometry optimization based on single crystals were calculated using the density functional theory (DFT) method at the M06-2X/6-31G(d,p) level of theory with the Gaussian 09 program package.<sup>31</sup> The excited states were calculated using the time-dependent density functional theory (TD-DFT) method at the M06-2X/6-31G(d,p) level of theory. The quantum theory of atoms in molecule (QTAIM) analysis was carried out for dimers in single crystals with the MultiWFN package (version 3.8),<sup>32</sup> based on single-point energy calculation at the M06-2X/6-31G(d,p) level of theory. The detailed calculation methods of energy decomposition analysis (EDA), hole-transfer integral ( $V$ ), reorganization energy ( $\lambda$ ), charge mobility ( $\mu$ ), and interaction energies ( $\Delta E$ ) are described in the Supporting Information.

**2.3. Characterization and Measurements.** The <sup>1</sup>H and <sup>13</sup>C NMR spectra were recorded on Bruker Avance 400 (400 and 100.6 MHz, respectively); chemical shifts are indicated in parts per million downfield from SiMe<sub>4</sub>, using the residual proton (CHCl<sub>3</sub> = 7.26 ppm) and carbon (CDCl<sub>3</sub> = 77.0 ppm) solvent resonances as the internal reference. Coupling constant values  $J$  are given in Hz. Thermogravimetric (TGA) measurements were carried out on TGA 4000 (PerkinElmer), with steady heating at a constant rate of 10 °C min<sup>-1</sup> under a constant nitrogen gas flow of 20 mL min<sup>-1</sup>. The investigated temperature intervals were between a minimum of 30 °C to a maximum of 900 °C. Ceramic crucibles and approximately 5–15 mg of sample material were used for each measurement. DSC curves were recorded on a DSC8000 calorimeter from PerkinElmer using 2–4 mg of sample powder placed in an

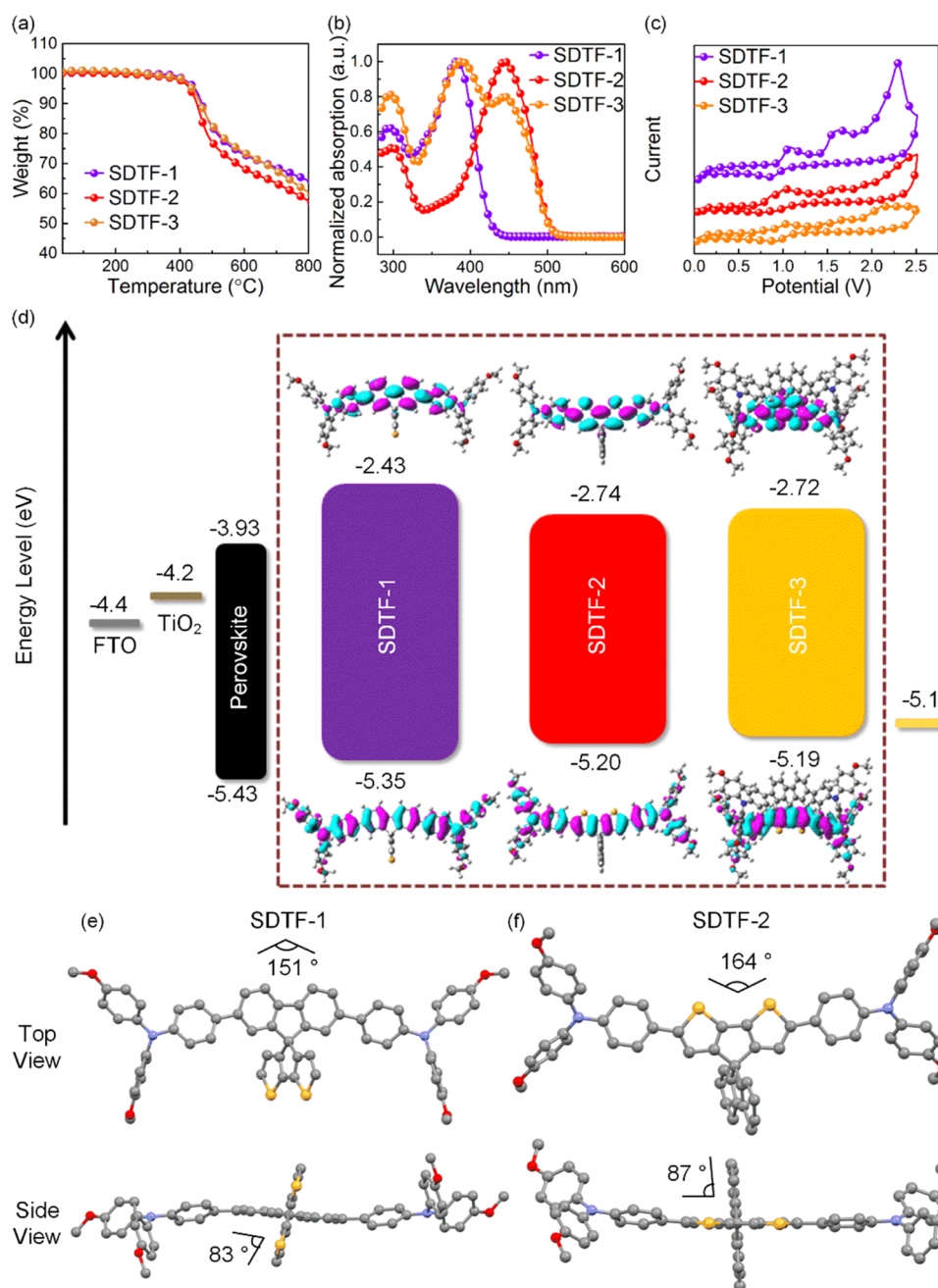


**Figure 2.** (a) TGA curves of SDTF-1, SDTF-2, and SDTF-3. (b) Normalized electronic absorption spectra of SDTF-1, SDTF-2, and SDTF-3 in dichloromethane solution. (c) Cyclic voltammograms of SDTF-1, SDTF-2, and SDTF-3 in dichloromethane with the 0.1 M Bu<sub>4</sub>NPF<sub>6</sub> supporting electrolyte. Scan speed: 100 mV/s, potentials vs Fc/Fc<sup>+</sup>. (d) Energy-level diagram for PSC device and the frontier molecular orbitals of SDTF-1, SDTF-2, and SDTF-3. ORTEP drawings of SDTF-1 (e) and SDTF-2 (f) determined by X-ray crystallography in top and side views.

aluminum pan with a tight-fitting lid. The scans were taken from  $-50$  to  $300$  °C at a rate of  $10$  °C min<sup>-1</sup> in a nitrogen atmosphere. Ultraviolet–visible (UV–vis) absorption spectra were recorded on a Nicolet Evolution 500 spectrophotometer (Thermo Electron Corporation). Cyclic voltammetry measurements were conducted with biologic SP200 potentiostat in deoxygenated 0.1 M dichloromethane solution of NBu<sub>4</sub>PF<sub>6</sub> under a nitrogen atmosphere. A glassy-carbon working electrode and platinum wire counter and reference electrodes were used. Measurements were carried out with ferrocene as an internal standard. The oxidation potential of ferrocene was positioned at 0.7 V vs normal hydrogen electrode (NHE)

potential, so the oxidation potential of HTMs was determined vs NHE.

**2.4. Device Fabrication.** Nippon Sheet Glass 10 Ω/sq was cleaned by sonication in 2% Hellmanex water solution for 30 min. After rinsing with deionized water and ethanol, the substrates were further cleaned with UV ozone treatment for 15 min. Then, a 30 nm TiO<sub>2</sub> compact layer was deposited on FTO via spray pyrolysis at 450 °C from a precursor solution of titanium diisopropoxide bis(acetylacetonate) in anhydrous ethanol. After the spraying, the substrates were left at 450 °C for 45 min and left to cool down to room temperature. Then, the mesoporous TiO<sub>2</sub> layer was deposited by spin coating for 20 s at 4000 rpm with a ramp of 2000 rpm s<sup>-1</sup>,

**Table 1.** Decomposition Temperatures, Optical Properties, Frontier Energy Levels, and Exciton Binding Energy of SDTF-1, SDTF-2, and SDTF-3

	$T_d$ [°C]	$\lambda_{\max}$ [nm] <sup>a</sup>	$\lambda_{\text{onset}}$ [nm] <sup>b</sup>	$E_g^{\text{opt}}$ [eV] <sup>c</sup>	$E_{\text{HOMO}}$ [eV] <sup>d</sup>	$E_{\text{LUMO}}$ [eV] <sup>e</sup>	$E_{\text{HOMO}}^{\text{cal}}$ [eV] <sup>f</sup>	$E_{\text{LUMO}}^{\text{cal}}$ [eV] <sup>f</sup>
SDTF-1	446	382	424	2.92	-5.35	-2.43	-4.49	-1.11
SDTF-2	431	445	504	2.46	-5.20	-2.74	-4.28	-1.40
SDTF-3	438	444	502	2.47	-5.19	-2.72	-4.22	-1.34

<sup>a</sup> $5 \times 10^{-5}$  M in dichloromethane solutions. <sup>b</sup>The absorption edge of the thin film. <sup>c</sup> $E_g^{\text{opt}} = 1240/\lambda_{\text{onset}}$  (eV). <sup>d</sup> $E_{\text{HOMO}} = -5.1 - (E_{\text{ox}} - E_{1/2}(\text{Fc}/\text{Fc}^+))$ . <sup>e</sup> $E_{\text{LUMO}} = E_g^{\text{opt}} - E_{\text{HOMO}}$ . <sup>f</sup>Calculated by DFT.

using a 30 nm particle paste (Dyesol 30 NR-D) diluted in ethanol to achieve a 150–200 nm thick layer. After spin coating, the substrates were immediately dried at 100 °C for 10 min and sintered again at 450 °C for 30 min under a dry air flow. Li-doping of mesoporous TiO<sub>2</sub> is accomplished by spin coating a 0.1 M solution of Li-TFSI in acetonitrile at 3000 rpm for 30 s, followed by another sintering step at 450 °C for 30 min. After cooling down to 150 °C, the substrates were immediately transferred to a nitrogen atmosphere glovebox for depositing the perovskite films. The “mixed perovskite” precursor solution contained FAI (1 M), PbI<sub>2</sub> (1.1 M), MABr (0.2 M), and PbBr<sub>2</sub> (0.2 M) dissolved in anhydrous DMF/DMSO 4:1 (v/v). The respective perovskite solution was spin coated in a two-step program at 1000 and 6000 rpm for 10 and 30 s, respectively. During the second step, 100  $\mu$ L of chlorobenzene was poured on the spinning substrate 15 s prior to the end of the program. The substrates were then annealed at 100 °C for 1 h in a nitrogen-filled glovebox. After the perovskite annealing, the substrates were cooled down for a few minutes and HTM (SDTF-1, SDTF-2, and SDTF-3) solutions (70 mM in chlorobenzene) were spin coated at 4000 rpm for 20 s. The HTMs were doped with bis-(trifluoromethylsulfanyl)imide lithium salt (Li-TFSI, Sigma-Aldrich), tris(2-(1*H*-pyrazol-1-yl)-4-*tert*-butylpyridine)-cobalt(III) tris(bis(trifluoromethylsulfanyl)imide) (FK209, Dynamo), and 4-*tert*-butylpyridine (TBP, Sigma-Aldrich). The molar ratios of additives for HTMs were 0.5, 0.03, and 3.3 for Li-TFSI, FK209, and TBP, respectively. Finally, 70–80 nm of the gold top electrode was thermally evaporated under a high vacuum.

**2.5. Device Characterization.** The solar cells were measured using a 450 W xenon light source (Oriel). The spectral mismatch between AM 1.5G and the simulated illumination was reduced by the use of a Schott K113 Tempax filter (Präzisions Glas & Optik GmbH). The light intensity was calibrated with a Si photodiode equipped with an infrared (IR)-cutoff filter (KG3, Schott), and it was recorded during each measurement. Current–voltage characteristics of the cells were obtained by applying an external voltage bias while measuring the current response with a digital source meter (Keithley 2400). The voltage scan rate was 10 mV s<sup>-1</sup> and no device preconditioning, such as light soaking or forward voltage bias applied for a long time, was applied before starting the measurement. The starting voltage was determined as the potential at which the cells furnished a 1 mA forward bias, no equilibration time was used. The cells were masked with a black metal mask (0.16 cm<sup>2</sup>) to fix the active area and reduce the influence of the scattered light. Aging under maximum power point tracking was carried out on masked devices, which were mounted on a temperature-controlled plate. The aging was performed under a nitrogen atmosphere and 50 sun equivalent illumination provided by an array of white light-emitting diodes (LEDs). The devices were aged by means of

keeping them under maximum load under illumination. The maximum power point was updated every 60 s by measuring the current response to a small perturbation in potential. Additionally, a full JV scan was taken every 15 min (at a scan rate of 100 mV s<sup>-1</sup> starting from the forward bias), which was used to extract the displayed parameters for the aging data.

### 3. RESULTS AND DISCUSSION

**3.1. Synthesis and Characterization.** The synthetic route for the target compounds is described in Figure 1. The key precursor brominated SDTF with different substitution modes (2',7'-dibromospiro[cyclopenta[2,1-*b*:3,4-*b'*]-dithiophene-4,9'-fluorene] (1), 2,6-dibromospiro[cyclopenta[2,1-*b*:3,4-*b'*]-dithiophene-4,9'-fluorene] (6) or 2,2',6,7'-tetrabromospiro[cyclopenta[2,1-*b*:3,4-*b'*]-dithiophene-4,9'-fluorene] (9)) can be obtained according to the previous work<sup>27</sup> and Experimental Section in the Supporting Information. SDTF-1, SDTF-2, and SDTF-3 were facily prepared by palladium-catalyzed Suzuki coupling between different brominated SDTF and 4-(bis(4-methoxyphenyl)amino)-phenylboronic acid (2) in high yields. The chemical structures of SDTF-1, SDTF-2, and SDTF-3 were confirmed by <sup>1</sup>H and <sup>13</sup>C nuclear magnetic resonance (NMR) (Figures S10–S25). These SDTF-based derivatives can be purified by standard column chromatography instead of costly sublimation procedures, as in the case of spiro-OMeTAD. This is relevant for industrial applications where large-scale chromatographic separation techniques are used. All of the compounds exhibited good solubility in common organic solvents such as chlorobenzene, toluene, tetrahydrofuran, and chloroform. Notably, the laboratory synthesis costs of SDTF-2 are estimated to be ~140 US\$ g<sup>-1</sup> (Tables S1 and S2), which is about half the cost of the synthesis of purified spiro-OMeTAD.

Thermal gravimetric analysis (TGA) and differential scanning calorimetry (DSC) were performed to investigate the thermal stability of these compounds. As shown in Figure 2a, the decomposition temperatures ( $T_d$ ) corresponding to 5% weight loss were estimated to be 446, 431, and 438 °C for SDTF-1, SDTF-2, and SDTF-3, respectively, which are higher than those of spiro-OMeTAD (417 °C),<sup>33</sup> indicating that all of the compounds have excellent thermal stability. The glass transition temperatures ( $T_g$ ) of three compounds (145, 150, and 179 °C for SDTF-1, SDTF-2, and SDTF-3, respectively) were much higher than that of spiro-OMeTAD (126 °C),<sup>33</sup> further confirming the good thermal stability (Figure S1). SDTF-3 exhibited the highest  $T_g$ , which can be ascribed to the improved rigidity of SDTF-3 molecules relative to the other two molecules.<sup>34</sup>

**3.2. Optical and Electrochemical Properties.** The normalized ultraviolet–visible (UV–vis) absorption spectra of SDTF-1, SDTF-2, and SDTF-3 in dichloromethane solutions are shown in Figure 2b, and the corresponding data are summarized in Table 1. The absorption peaks in the

280–340 nm region can be attributed to the  $n-\pi^*$  transition of triphenylamine moieties. The intense absorption peaks in the region of 350–510 nm can be assigned to the  $\pi-\pi^*$  transition of the triphenylamine and SDTF moieties. In comparison, changing the linkage position at cyclopentadithiophene instead of fluorene leads to a significant red-shift, indicating a reduced optical band gap due to the lower resonance energy of thiophene rings.<sup>19,26</sup> SDTF-2 and SDTF-3 with a smaller band gap show enhanced intrinsic electrical conductivity due to the increased carrier concentration.<sup>35–37</sup>

Cyclic voltammograms (CVs) of SDTF-1, SDTF-2, and SDTF-3 were performed in dichloromethane solution to study the electrochemical properties of the three compounds, as depicted in Figure 2c. The highest occupied molecular orbital (HOMO) energy levels ( $E_{\text{HOMO}}$ ) were estimated from the half-wave oxidation potential of the first oxidation peak, considering the ferrocenium/ferrocene couple at  $-5.1$  eV vs vacuum.<sup>38</sup> The first oxidation peak of SDTF-1, SDTF-2, and SDTF-3 are 0.95, 0.80, and 0.79 V vs the normal hydrogen electrode (NHE), respectively. Thus, the estimated values of  $E_{\text{HOMO}}$  are  $-5.35$  eV for SDTF-1,  $-5.20$  eV for SDTF-2, and  $-5.19$  eV for SDTF-3. These HOMO energy levels match well with the valence band of perovskite (Figure 2d), ensuring efficient hole extraction from the perovskite layer to HTM. On the other hand, the lowest unoccupied molecular orbital (LUMO) levels ( $E_{\text{LUMO}}$ ) of SDTF-1, SDTF-2, and SDTF-3 were determined from  $E_{\text{HOMO}}$  and  $E_{\text{g}}^{\text{opt}}$  values to be  $-2.43$ ,  $-2.74$ , and  $-2.72$  eV, respectively. They are higher than the conduction band of the perovskite, preventing the electron backflow from the perovskite layer to the counter electrode.

**3.3. Electronic Structure.** To understand the electronic properties of the three compounds, density functional theory (DFT) calculations were performed at the M06-2X/6-31G(d,p) level. The frontier molecular orbitals of SDTF-1, SDTF-2, and SDTF-3 are depicted in Figure 2d. The HOMO distribution is concentrated on the TPAs and linking spacers (fluorene for SDTF-1 and cyclopentadithiophene for SDTF-2, respectively), while the LUMO is mainly distributed on the corresponding linking spacers. This indicates the migration charge from the peripheral TPAs to the central SDTF core. It is worth noting that the frontier molecular orbital distributions of SDTF-3 are very similar to those of SDTF-2, which can be ascribed to the stronger electron-donating ability of cyclopentadithiophene relative to fluorene. The calculated HOMO/LUMO energy levels of the compounds are  $-4.49/-1.11$  eV for SDTF-1,  $-4.28/-1.40$  eV for SDTF-2, and  $-4.22/-1.34$  eV for SDTF-3. This trend is well consistent with the experimental results. The difference between the calculated and measured HOMO/LUMO energy levels may be because the calculated energy levels were determined in the gas phase. In contrast, cyclic voltammetry measured the experimental energy levels in the dichloromethane solution. Moreover, some environmental factors, including temperature, humidity, oxygen, etc., are not involved in the calculation. In addition, there is an error in the computational method itself, and the energy levels calculated by combining different functionals and basis sets are different.

In addition, the exciton binding energy ( $E_{\text{b}}$ ) is also an essential factor in describing the charge separation efficiency of the HTMs.<sup>39,40</sup> To achieve high carrier transport, the bound electron–hole pairs should be dissociated into wholly separated positive and negative charges to escape from the Coulombic interaction.<sup>41</sup> The  $E_{\text{b}}$  is the energy difference

between the neutral exciton and the two free charge carriers, which can be described as<sup>40,42</sup>

$$E_{\text{b}} = E_{\text{H-L}} - E_{\text{S1}} \quad (1)$$

where  $E_{\text{H-L}}$  is the energy difference between the HOMO and the LUMO and  $E_{\text{S1}}$  is the first singlet excitation energy. We used the time-dependent DFT (TD-DFT) method to investigate the  $E_{\text{S1}}$ , and the relevant data are summarized in Table 2. In PSCs, the smaller  $E_{\text{b}}$  represents the easier charge

**Table 2. Calculated Exciton Binding Energy and Ionization Potentials of SDTF, SDTF-2, and SDTF-3**

	$E_{\text{H-L}}$ [eV]	$E_{\text{S1}}$ [eV]	$E_{\text{b}}$ [eV]	Ip ( $\nu$ ) [eV] <sup>a</sup>	Ip ( $a$ ) [eV] <sup>b</sup>	HEP [eV]
SDTF-1	3.38	2.97	0.41	6.03	5.94	5.85
SDTF-2	2.88	2.54	0.34	5.93	5.87	5.82
SDTF-3	2.88	2.53	0.35	5.75	5.67	5.58

<sup>a</sup> $\nu$  indicates a vertical value. <sup>b</sup> $a$  indicates an adiabatic value.

separation to improve the short-circuit current density and carrier mobility. The  $E_{\text{b}}$  values of SDTF-1, SDTF-2, and SDTF-3 are 0.41, 0.34, and 0.35 eV, respectively. The lower  $E_{\text{b}}$  values of SDTF-2 and SDTF-3 suggest that introducing TPAs on cyclopentadithiophene facilitates easier charge carrier dissociation.

The ionization potential (IP) is used to estimate the energy barrier for the injection of holes.<sup>43,44</sup> Table 2 contains IPs, both vertical and adiabatic forms, and hole extraction potentials (HEP) (the energy difference between the cationic and neutral states based on the optimized geometry of the cationic states).<sup>43</sup> Theoretically, the lower IP value is favorable for hole injection/transport. As predicted, SDTF-2 has lower IPs than SDTF-1, indicating that cyclopentadithiophene has a better electron-donating ability to facilitate hole injection/transport for SDTF-2. This result agrees well with the analysis above. On the other hand, SDTF-3 has the lowest IPs due to the introduction of more TPAs.

**3.4. Single-Crystal Structure and Intermolecular Interaction.** To understand how the variation of linkage position impacts the solid-state molecular stacking, single crystals of SDTF-1 and SDTF-2 suitable for X-ray diffraction analysis were grown via slow evaporation in the THF solution. Unfortunately, in the case of SDTF-3, no suitable single crystal was obtained. The refined crystal parameters are collected in Table S3 in the Supporting Information.

The compounds crystallized in the orthorhombic  $Pccn$  space group for SDTF-1 and monoclinic  $P2_1$  space group for SDTF-2. As shown in Figure 2e,f, for SDTF-2, when the TPAs are substituted on the cyclopentadithiophene part of SDTF-2, the bending angle of the two C–N bonds is measured to be  $164^\circ$ , which is slightly bigger than that of SDTF-1 ( $151^\circ$ ) with two TPAs on fluorene. The optimized structure of SDTF-3 by DFT calculations is given in Figure S2. The bending angles of the two C–N bonds with TPAs on cyclopentadithiophene and fluorene are  $168$  and  $157^\circ$ , respectively. This is similar to the single-crystal structure of SDTF-1 and SDTF-2. At the same time, the dihedral angles between fluorene and cyclopentadithiophene were measured to be  $83$ ,  $87$ , and  $90^\circ$  for SDTF-1, SDTF-2, and SDTF-3, respectively (Figures 2e,f and S2). This is similar to the value found for ubiquitous Spiro-OMeTAD ( $\sim 90^\circ$ )<sup>45</sup> and FDT ( $86^\circ$ ),<sup>27</sup> which indicates that unwanted aggregation in the solid state could be suppressed,

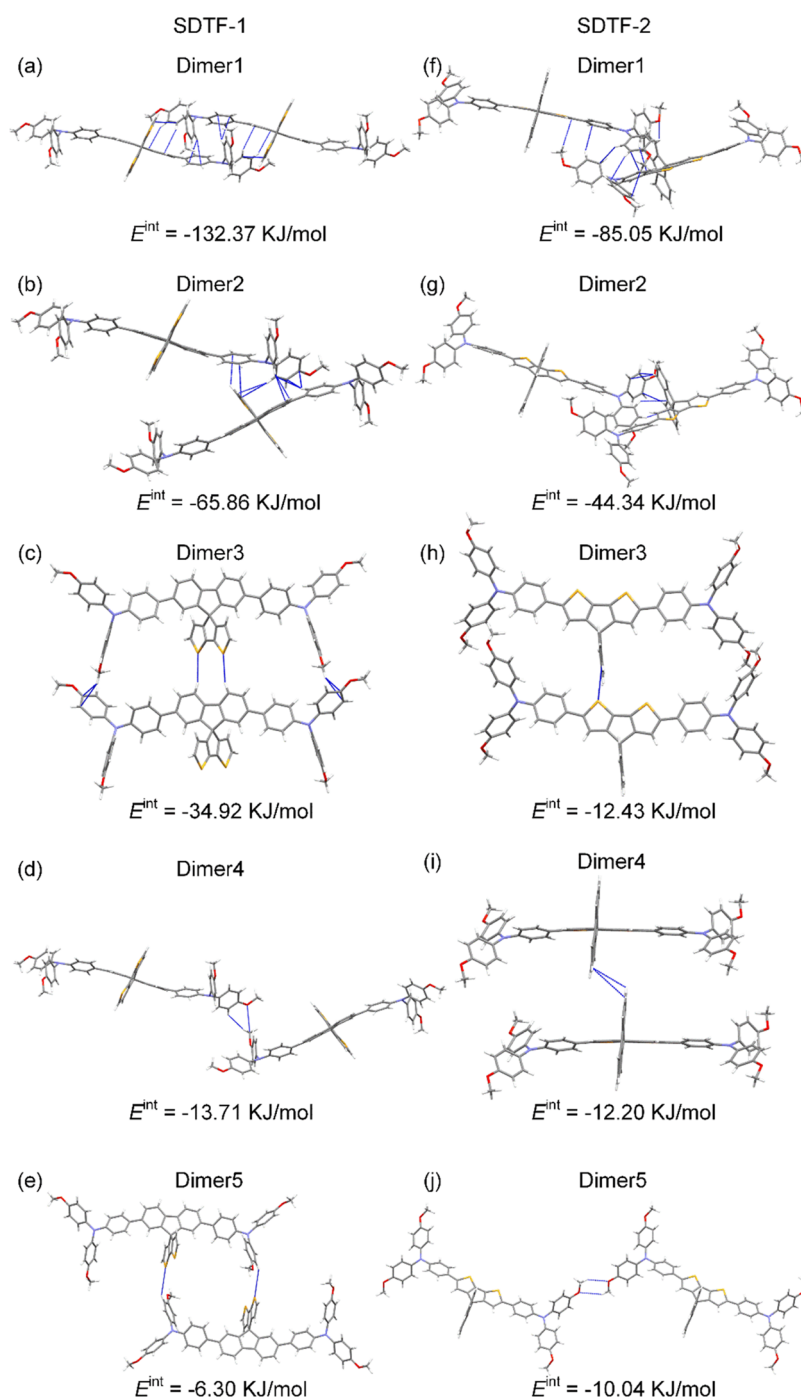


**Figure 3.** Molecular packing structures and interaction energies of dimers 1–5 extracted from (a–e) SDTF-1 and (f–j) SDTF-2 single crystals.

and a more stable amorphous aggregation state tends to be formed.

To clarify the intermolecular noncovalent interactions (NCIs) in organic solids that control molecular arrangement, all types of dimers composed of two neighboring molecules were extracted from single-crystal structures of SDTF-1 and SDTF-2 and not constructed arbitrarily. Theoretical calculations based on the quantum theory of atoms in molecules (QTAIMs) were then carried out to elaborate on the essential features and bond paths of various NCIs.<sup>46–51</sup> Energy decomposition analysis (EDA) on each dimer was also performed to quantify the total interaction energy ( $E^{\text{int}}$ ).<sup>52</sup> Here,  $E^{\text{int}}$  is defined as the sum of electrostatic energy ( $E^{\text{ele}}$ ),

repulsion energy ( $E^{\text{rep}}$ ), and dispersion energy ( $E^{\text{disp}}$ ). For details, see Tables S4 and S5 in the Supporting Information.

The SDTF-1 single crystal has four molecules in a primitive unit cell. The structures in different directions are shown in Figure S3. We extracted five types of dimers from the single-crystal structure of SDTF-1. Along the *b*-axis, two neighboring SDTF-1 molecules can form two types of dimers, i.e., dimer 1 (Figure 3a) and dimer 2 (Figure 3b), with  $E^{\text{int}}$  values of 132.37 and 65.86 kJ/mol, respectively. Dimers 1 and 2 have the top two largest  $E^{\text{int}}$  values among all of the five dimers of SDTF-1. The  $E^{\text{int}}$  value of dimer 3 with two cross-parallel conformations along the *c*-axis is reduced to 34.92 kJ/mol (Figure 3c). The  $E^{\text{int}}$  values of dimer 4 with two diverse conformations along the

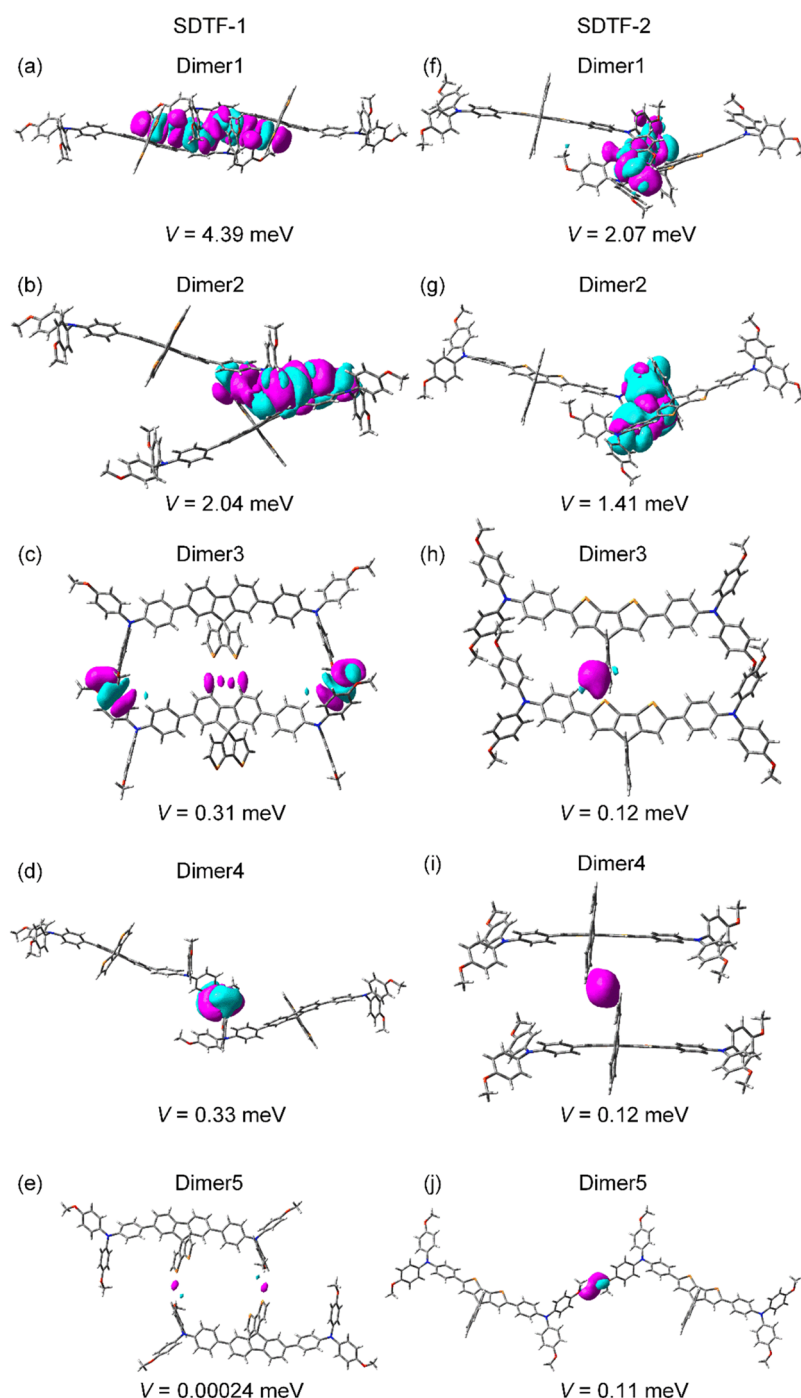


**Figure 4.** Isodensity surface plots of intermolecular HOMO overlaps of dimers 1–5 extracted from (a–e) SDTF-1 and (f–j) SDTF-2 single crystals.

*a*-axis and dimer 5 with two antiparallel conformations are calculated to be 13.71 and 6.30 kJ/mol, respectively (Figure 3d,e), which are significantly smaller compared to those of other dimers. The results of QTAIM analysis suggest the existence of multiple NCIs among these dimers: (i)  $\pi$ – $\pi$  interaction between the methoxyphenyl  $\pi$ -skeleton and the cyclopentadithiophene  $\pi$ -skeleton (dimers 1 and 2), (ii) CH– $\pi$  interaction between the methoxyphenyl aromatic CH and the fluorene  $\pi$ -skeleton (dimer 1), (iii) CH– $\pi$  interaction between the methoxyphenyl aromatic CH and the triphenylamine phenyl  $\pi$ -skeleton (dimer 1), (iv) CH– $\pi$  interaction between the cyclopentadithiophene CH and the triphenyl-

amine phenyl  $\pi$ -skeleton (dimer 2), (v) CH– $\pi$  interaction between the triphenylamine phenyl CH and the methoxyphenyl  $\pi$ -skeleton (dimer 2), (vi) CH– $\pi$  interaction between the methoxyphenyl aliphatic CH and the methoxyphenyl  $\pi$ -skeleton (dimer 3), (vii) S–H interaction between the cyclopentadithiophene S and the fluorene CH (dimer 3), (viii) S–H interaction between the cyclopentadithiophene S and the methoxyphenyl aromatic CH (dimer 5), (ix) O–H interaction between the methoxyphenyl O and the methoxyphenyl aromatic CH (dimer 4), and (x) H–H interaction between the methoxyphenyl aromatic CH and the methoxyphenyl aliphatic CH (dimer 4).

In contrast, the single crystal of **SDTF-2** is characterized as an antiparallel dimer in one unit cell, featuring a “brick-layer stacking” mode along the long molecular axis (Figure 3f). The structures in different directions are shown in Figure S4. Similarly, five types of dimers were extracted from the single-crystal structure of **SDTF-2**. As shown in Figure 3f, the  $E^{\text{int}}$  value of dimer 1, consisting of a primitive unit cell of **SDTF-2**, is calculated to be 85.05 kJ/mol, much larger than those of the other four dimers. Dimer 2 with  $E^{\text{int}} = 44.34$  kJ/mol (Figure 3g) and dimer 3 with  $E^{\text{int}} = 12.43$  kJ/mol (Figure 3h) are formed with adjacent molecules belonging to two primitive unit cells along the *c*-axis. The  $E^{\text{int}}$  values of dimer 4 and dimer 5 with two parallel conformations along the *a*- and *b*-axis are calculated to be 12.20 and 10.04 kJ/mol, respectively (Figure 3i,j). Based on the QTAIM analysis, 10 types of NCI are found in these dimers, including (i)  $\pi$ - $\pi$  interaction of the methoxyphenyl  $\pi$ -skeleton (dimer 1), (ii) CH- $\pi$  interaction between the methoxyphenyl aliphatic CH and the cyclopentadithiophene  $\pi$ -skeleton (dimer 1), (iii) CH- $\pi$  interaction between the methoxyphenyl aromatic CH and the triphenylamine phenyl  $\pi$ -skeleton (dimer 1), (iv) CH- $\pi$  interaction between the methoxyphenyl aliphatic CH and the methoxyphenyl  $\pi$ -skeleton (dimer 1), (v) CH- $\pi$  interaction between the methoxyphenyl aromatic CH and the fluorene  $\pi$ -skeleton (dimer 2), (vi) CH- $\pi$  interaction between the fluorene CH and the methoxyphenyl  $\pi$ -skeleton (dimer 2), (vii) O-H interaction between the methoxyphenyl O and the fluorene CH (dimer 1), (viii) S-H interaction between the cyclopentadithiophene S and the fluorene CH (dimer 3), (ix) H-H interaction of the fluorene CH (dimer 4), and (x) O-H interaction between the methoxyphenyl O and the methoxyphenyl aliphatic CH (dimer 5).

To study NCIs of **SDTF-3**, we carried out the stable **SDTF-3** single crystal predictions using the polymorph module in the Materials Studio program package. The **SDTF-3** single crystal has four molecules in a primitive unit cell. The structures in different directions are shown in Figure S5. Five types of dimers for **SDTF-3** were extracted based on the predicted crystal structure. As shown in Figure S6a-e, the  $E^{\text{int}}$  values of dimers 1-5 are much smaller than those of **SDTF-1** and **SDTF-2**. Along the *c*-axis, two neighboring **SDTF-3** molecules can form dimer 1 belonging to two primitive unit cells with an  $E^{\text{int}}$  value of 18.09 kJ/mol. Dimer 2 with  $E^{\text{int}} = 17.44$  kJ/mol and dimer 3 with  $E^{\text{int}} = 4.95$  kJ/mol are formed with adjacent molecules belonging to one primitive unit cell. The  $E^{\text{int}}$  values of dimer 4 and dimer 5 belonging to two primitive unit cells along the *a*- and *b*-axis are calculated to be 0.94 and 0.26 kJ/mol, respectively, which are much smaller than those of the other three dimers. Multiple NCIs can be found in Figure S6 for the predicted **SDTF-3** crystal structure, including four forms of interaction: (i) CH- $\pi$  interaction between the methoxyphenyl aliphatic CH and the methoxyphenyl  $\pi$ -skeleton (dimers 2 and 3), (ii) CH- $\pi$  interaction between the methoxyphenyl aliphatic CH and the triphenylamine phenyl  $\pi$ -skeleton (dimer 2), (iii) O-H interaction between the methoxyphenyl O and methoxyphenyl CH (dimer 1), and (iv) H-H interaction between the methoxyphenyl aliphatic CH and the methoxyphenyl CH (dimer 2). Note that the  $\pi$ - $\pi$  interaction does not exist in the **SDTF-3** crystal structure.

**3.5. Reorganization Energy, Transfer Integral, and Hole Mobility.** Generally, the high hole-transporting ability of HTMs helps improve the performance of PSCs. Theoretically, the hole transport in organic semiconductors can be viewed as

a self-exchange hopping process, that is, a hole transfer between two adjacent molecules.<sup>53,54</sup> The process can be accounted for by the Marcus theory, and the hole hopping rate ( $k_{\text{hole}}$ ) is estimated by the following equations<sup>55</sup>

$$k_{\text{hole}} = \frac{4\pi^2 V^2}{h} \frac{1}{\sqrt{4\pi\lambda k_{\text{B}} T}} \exp\left[-\frac{\lambda}{4k_{\text{B}} T}\right] \quad (2)$$

where  $V$  is the hole-transfer integral between adjacent molecules in a single-crystal structure,  $\lambda$  is the reorganization energy,  $h$  is the Planck constant,  $k_{\text{B}}$  is the Boltzmann constant, and  $T$  is the temperature in kelvin. Apparently, the  $k_{\text{hole}}$  is influenced by two critical parameters of  $V$  and  $\lambda$ . The large  $V$  and the small  $\lambda$  favor the hole transport in HTMs. Herein, DFT calculations were performed at the M06-2X/6-31G(d,p) level to investigate the  $V$  and  $\lambda$  of **SDTF-1**, **SDTF-2**, and **SDTF-3** based on the extracted dimers in single-crystal structures. The calculated  $V$  and  $\lambda$  are depicted in Figures 4 and S6 and Tables S7-S9.

$V$  is dependent on the HOMO wavefunction overlap. As shown in Figure 4a,b, in the **SDTF-1** single crystal, dimers 1 and 2, which are composed of two adjacent molecules, possess a remarkable HOMO overlap due to the strong  $\pi$ - $\pi$  and CH- $\pi$  interaction and thereby give large  $V$  values of 4.39 and 2.04 meV, respectively. On the contrary, for dimers 3 and 4, the HOMO overlaps are attenuated, mainly located on the methoxyphenyl moiety, and their  $V$  values are reduced to 0.31 and 0.33 meV, respectively (Figure 4c,d). Unfortunately, the little HOMO overlap of cyclopentadithiophene and methoxyphenyl can be noted for dimer 5 owing to the considerable distance of 4.22 Å between S and H atoms, the  $V$  value of which virtually approaches zero (Figure 4e).

Similarly, in the **SDTF-2** single crystal, the HOMO overlaps of two adjacent molecules are observed for dimers 1 and 2, which are mainly contributed by the TPA and fluorene moieties. As a result, the  $V$  values of dimers 1 and 2 are 2.07 and 1.41 meV, respectively (Figure 4f,g). In contrast, the  $V$  values of the other three dimers (dimers 3-5) are remarkably diminished, dropping to  $\sim 0.12$  meV (Figure 4h-j). This is because only “edge-to-edge” interactions exist in the three dimers, resulting in a tiny HOMO overlap. In addition, it is noted that the electronic coupling strengths in the three dimers along different directions are of the same order of magnitude, proving the multidimensional charge-transfer pathways.

Unfortunately, based on the predicted **SDTF-3** crystal structure, the HOMO overlaps for dimers 1-5 are all located on the methoxyphenyl moiety, and the distance between two adjacent molecules is relatively large, which results in the  $V$  values of dimers 1-5 to be very small (the  $V$  values of dimers 4 and 5 are close to zero) (Figure S6f-j).

Typically,  $\lambda$  is composed of internal reorganization energy ( $\lambda_{\text{int}}$ ) and external reorganization energy ( $\lambda_{\text{ext}}$ ).  $\lambda_{\text{int}}$  is a measure of the structural change between ionic and neutral states.<sup>53</sup>  $\lambda_{\text{ext}}$  represents the effect of the polarized medium on charge transfer.<sup>53</sup> For most organic molecules,  $\lambda_{\text{ext}}$  can be neglected because of its little contribution to the solid state.<sup>56</sup> Therefore, in this work, only  $\lambda_{\text{int}}$  is obtained ( $\lambda \approx \lambda_{\text{int}}$ ), ignoring the impact of the external environment. The internal part depends on the change of molecular geometry during the hole-transfer process. According to the calculations of various geometry energies,  $\lambda_{\text{int}}$  for hole transfer can ultimately be expressed as the following formula<sup>43</sup>

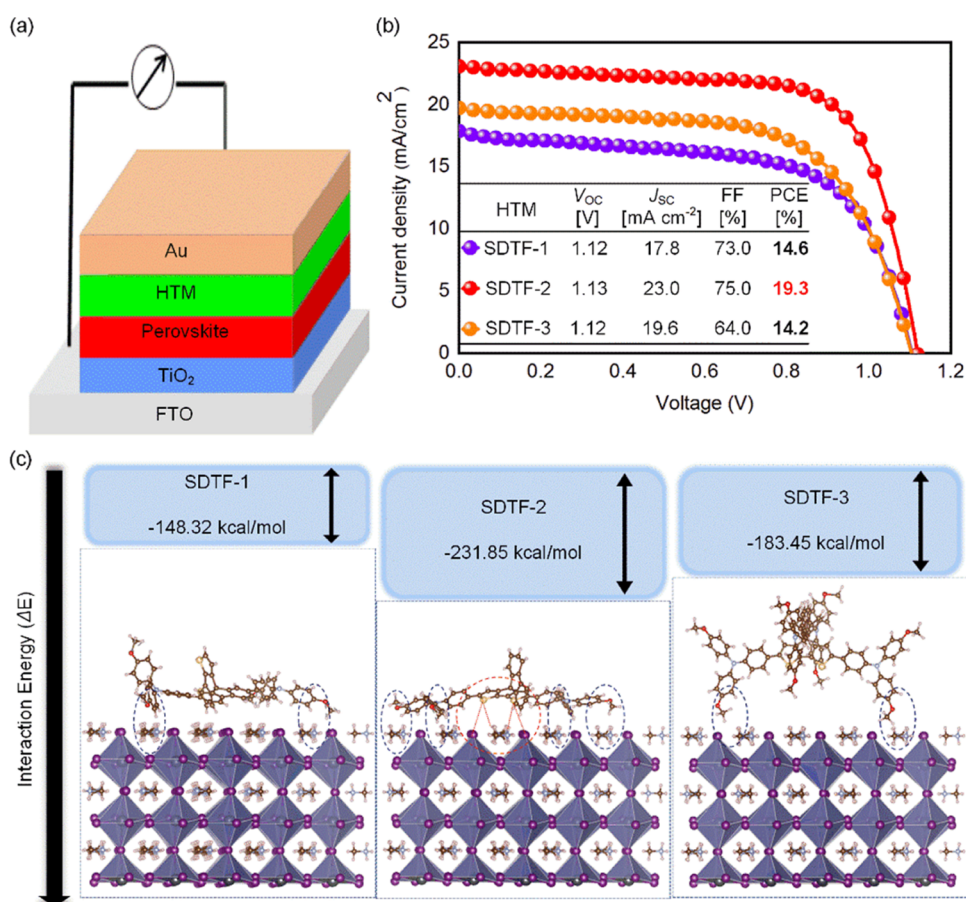


**Figure 5.** (a) Schematic illustration of the device configuration. (b)  $J$ - $V$  curves of PSCs employing SDTF-1, SDTF-2, and SDTF-3 as HTMs. (c) DFT calculation of the interaction energies between SDTF-1, SDTF-2, and SDTF-3 and the exposed MAI-terminated surface.

$$\lambda \approx \lambda_{\text{int}} = \text{IP}(\nu) - \text{HEP} \quad (3)$$

The calculated  $\lambda$  value of SDTF-2 is 110 meV, which is smaller than 180 meV for SDTF-1 and 170 meV for SDTF-3. The smaller  $\lambda$  implies better hole transportability for SDTF-2. It is worth noting that the  $\lambda$  values of the three compounds are much larger than any transfer integrals. We can infer that hole transport in SDTF-1, SDTF-2, and SDTF-3 single crystals are governed by hole hopping.<sup>34,47,48,50</sup> According to the calculated  $\lambda$ , the hole mobility ( $\mu$ ) of SDTF-1, SDTF-2, and SDTF-3 can be obtained using the Einstein equation<sup>40,50</sup>

$$\mu = \frac{eD}{k_B T} \quad (4)$$

where  $e$  is the elementary charge,  $D$  is the diffusion coefficient,  $k_B$  is the Boltzmann constant, and  $T$  is the temperature in kelvin. For calculation details, see [Experimental Section](#) in the Supporting Information. The predicted theoretical  $\mu$  at room temperature is  $1.11 \times 10^{-2} \text{ cm}^2 \text{ V}^{-1} \text{ s}^{-1}$  for SDTF-2, which is higher than those of SDTF-1 ( $9.11 \times 10^{-3} \text{ cm}^2 \text{ V}^{-1} \text{ s}^{-1}$ ) and SDTF-3 ( $1.02 \times 10^{-4} \text{ cm}^2 \text{ V}^{-1} \text{ s}^{-1}$ ). Although the total transfer integral of SDTF-2 (3.83 meV) is smaller than that of SDTF-1 (7.07 meV), the significantly reduced  $\lambda$  generates an even higher theoretical hole mobility for SDTF-2.

**3.6. Photovoltaic Performance.** In a PSC device, the hole-transporting materials (HTMs) play a critical role in facilitating hole extraction and protecting the perovskite layer from external degradation, such as moisture.<sup>57–63</sup> To evaluate the potential of SDTF-1, SDTF-2, and SDTF-3 as HTMs in

PSCs, devices with the structure of FTO/TiO<sub>2</sub>/perovskite/HTM/Au were fabricated ([Figure 5a](#)). Details of the device fabrication can be found in the [Supporting Information](#). The current density–voltage ( $J$ - $V$ ) curves under the standard AM 1.5G illumination of champion cells are shown in [Figure 5b](#). The best SDTF-1/SDTF-3-based device exhibits a moderate power conversion efficiency (PCE) of 14.6/14.2% with an open-circuit voltage ( $V_{oc}$ ) of 1.12/1.12 V, short-circuit photocurrent ( $J_{sc}$ ) of 17.8/19.6  $\text{mA cm}^{-2}$ , and fill factor (FF) of 73/64%. Encouragingly, SDTF-2-based devices show a significantly enhanced PCE of up to 19.3% ( $V_{oc}$  of 1.13 V,  $J_{sc}$  of 23.0  $\text{mA cm}^{-2}$ , and FF of 75%), which is also confirmed statistically in [Figure S7](#). Generally, the hole mobility of HTMs plays an important role in determining the  $J_{sc}$ .<sup>61,64,65</sup> Compared with SDTF-1 and SDTF-3, the higher  $J_{sc}$  of SDTF-2 can be explained by the higher hole mobility and better hole extraction, which agrees with the results from theoretical calculations. However, the effect of HTMs on  $V_{oc}$  is complex. This is because the  $V_{oc}$  loss may originate from the energy alignment, film-forming property, and interfacial contact.<sup>59,66</sup> In theory, a deeper HOMO energy level of HTM can contribute to a larger  $V_{oc}$  if sufficient driving force for hole extraction is guaranteed.<sup>67,68</sup> There is no evident difference in  $V_{oc}$  between SDTF-2- and SDTF-3-based devices, which can be explained by the fact that SDTF-2 and SDTF-3 have almost the same HOMO energy levels ( $-5.20$  and  $-5.19$  eV, respectively). Unexpectedly, although SDTF-1 has a downshifted HOMO energy level ( $-5.35$  eV), SDTF-1-

based device exhibited almost the same  $V_{OC}$  of 1.12 V as those of SDTF-2 and SDTF-3 (1.13 and 1.12 V, respectively). We suppose that the enhanced  $V_{OC}$  loss may come from the poor film-forming property and interfacial contact.<sup>69</sup> We also measured the photovoltaic characteristics of PSCs based on spiro-OMeTAD as a benchmark (Figure S8 and Table S10). It is worth mentioning that the photovoltaic performance of the SDTF-2-based device is on par with that of the spiro-OMeTAD-based device (PCE = 19.7%). In addition, the device stabilities based on SDTF-2 and spiro-OMeTAD were investigated, as shown in Figure S9. The aging test was carried out under continuous 50 sun exposure generated by an LED light source in a nitrogen atmosphere at room temperature. The performance of the devices was tracked under the maximum power point (MPP) condition. Both SDTF-2- and spiro-OMeTAD-based devices exhibit a similar degradation mechanism, e.g., a faster degradation during the  $\sim 3000$  s, followed by a slower decay until  $\sim 9000$  s, retaining  $\geq 80\%$  of their initial PCE. The results reveal that the devices employing SDTF-2 as the HTM show similar stability behavior to those of spiro-OMeTAD as the state-of-the-art HTM under the same conditions.

The first-principles calculation has been performed based on DFT to understand better the profound difference between SDTF-1-, SDTF-2-, and SDTF-3-based device performances. We utilized a combined cluster and periodic model (MAPbI<sub>3</sub>) approach to reveal the HTM/perovskite interaction. According to previous reports, the simulation study on the surface interaction between the methoxy-containing molecule (e.g., spiro-OMeTAD) and MAPbI<sub>3</sub> revealed that the methoxy group adsorbed to the surface of perovskite via the interaction with methylammonium cation was governed by electrostatic interaction.<sup>70</sup> In particular, we modeled the SDTF-1, SDTF-2, and SDTF-3 molecules onto the exposed MAI of the perovskite cluster surface (010). The optimized geometries and interaction energy of the two HTM/perovskite interfaces are shown in Figure 5c, and the detailed simulation results can be obtained in the Supporting Information. As shown in Figure 5c, the molecular geometries of the perovskite surface can be strongly affected by coupling different positions of TPAs. All of the methoxy oxygen atoms of SDTF-2 can easily form a strong interaction with the MA<sup>+</sup> cations of the perovskite surface via hydrogen bonding (highlighted by the blue circle in Figure 5c), while SDTF-1 and SDTF-3 molecules can only contribute two oxygen atoms to bind with MA<sup>+</sup> cations. It is worth noting that the additional interaction occurred between the sulfur atoms of SDTF-2 and MA<sup>+</sup> cations or iodine atoms of the perovskite surface (highlighted by the red circle in Figure 5c). This may suggest a stronger adhesion and enhanced interfacial coupling between cyclopentadithiophene of SDTF-2 and perovskite.<sup>27,71</sup> The additional thiophene–iodine interaction may provide an alternative hole-transfer pathway, which is favorable for effective hole extraction at the perovskite interface. This can be further confirmed by comparing the interaction energies ( $\Delta E$ ) of the three molecules with perovskite: SDTF-2 has a strongly favored interaction energy ( $\Delta E = -231.85$  kcal/mol) compared to those of SDTF-1 ( $\Delta E = -148.32$  kcal/mol) and SDTF-3 ( $\Delta E = -183.45$  kcal/mol). The strong binding correlation significantly increases the stability of the SDTF-2/perovskite interface. This higher stability also suggests a more compact layer generated by SDTF-2, which can restrain the methylammonium cations and iodine atoms from moving on the surface and further reduce the charge recombination.

These results could explain why the devices with cyclopentadithiophene-linked SDTF-2 exhibit higher PCE than those with only fluorene-linked SDTF-1 and cyclopentadithiophene fluorene-linked SDTF-3-based solar cells.

#### 4. CONCLUSIONS

In summary, we present the synthesis and a systematic study of the effect of three SDTF-based hole-transporting materials on the photovoltaic performance of PSCs. The position of triphenylamine substitution on the SDTF core notably impacts the thermal, optical, and electrochemical properties. The combined computational analysis based on the single-crystal structure elucidated the difference in electronic structures, exciton binding energies, ionization potentials, intermolecular interaction energy, and hole mobilities of the studied HTMs. Furthermore, the reduced band gap (2.46 eV), lower exciton binding energy (0.34 eV), and higher theoretical hole mobility ( $1.11 \times 10^{-2}$  cm<sup>2</sup> V<sup>-1</sup> s<sup>-1</sup>) of SDTF-2 resulted in a higher open-circuit voltage and significantly improved short-circuit current. Thus, we show that hole transportability can be tuned by altering the substitution position of the SDTF core.

Furthermore, the PSC device fabricated with SDTF-2 as the HTM displayed the highest power conversion efficiency of 19.3%, which is on par with the spiro-OMeTAD-based device. Moreover, DFT calculations revealed that the tight hole extraction partially originated from the strong interaction between the SDTF-2 molecule and MAI at the perovskite surface. Consequently, variation in linking topology proves to tune SDTF-based HTMs for PSCs effectively. Hopefully, this theoretical approach can provide guidelines for further developing high-performance HTMs in PSCs.

#### ■ ASSOCIATED CONTENT

##### Supporting Information

The Supporting Information is available free of charge at <https://pubs.acs.org/doi/10.1021/acs.jpcc.2c06152>.

Crystal data (ZIP)

Detailed description of the experimental methods, including molecular synthesis, theoretical calculations, additional data and figures, NMR spectra, etc (PDF)

#### ■ AUTHOR INFORMATION

##### Corresponding Authors

**Simonetta Orlandi** – Institute of Chemical Sciences and Technologies “Giulio Natta” of National Research Council, I-20133 Milano, Italy; [orcid.org/0000-0001-6783-4243](https://orcid.org/0000-0001-6783-4243); Email: [simonetta.orlandi@scitec.cnr.it](mailto:simonetta.orlandi@scitec.cnr.it)

**Michael Saliba** – Institute for Photovoltaics (ipv), University of Stuttgart, 70569 Stuttgart, Germany; Helmholtz Young Investigator Group FRONTRUNNER, 52425 Jülich, Germany; [orcid.org/0000-0002-6818-9781](https://orcid.org/0000-0002-6818-9781); Email: [michael.saliba@ipv.uni-stuttgart.de](mailto:michael.saliba@ipv.uni-stuttgart.de)

**Peng Gao** – CAS Key Laboratory of Design and Assembly of Functional Nanostructures, and Fujian Provincial Key Laboratory of Nanomaterials Fujian Institute of Research on the Structure of Matter, Chinese Academy of Sciences, Fuzhou, Fujian 350002, China; Xiamen Key Laboratory of Rare Earth Photoelectric Functional Materials, Xiamen Institute of Rare Earth Materials, Haixi Institute, Chinese Academy of Sciences, Xiamen 361021, China; [orcid.org/0000-0002-4963-2282](https://orcid.org/0000-0002-4963-2282); Email: [peng.gao@fjirsm.ac.cn](mailto:peng.gao@fjirsm.ac.cn)

## Authors

Zilong Zhang – CAS Key Laboratory of Design and Assembly of Functional Nanostructures, and Fujian Provincial Key Laboratory of Nanomaterials Fujian Institute of Research on the Structure of Matter, Chinese Academy of Sciences, Fuzhou, Fujian 350002, China; Xiamen Key Laboratory of Rare Earth Photoelectric Functional Materials, Xiamen Institute of Rare Earth Materials, Haixi Institute, Chinese Academy of Sciences, Xiamen 361021, China

Wenbo Li – CAS Key Laboratory of Design and Assembly of Functional Nanostructures, and Fujian Provincial Key Laboratory of Nanomaterials Fujian Institute of Research on the Structure of Matter, Chinese Academy of Sciences, Fuzhou, Fujian 350002, China; Xiamen Key Laboratory of Rare Earth Photoelectric Functional Materials, Xiamen Institute of Rare Earth Materials, Haixi Institute, Chinese Academy of Sciences, Xiamen 361021, China

Marco Cavazzini – Institute of Chemical Sciences and Technologies “Giulio Natta” of National Research Council, I-20133 Milano, Italy

Abdullah M. Asiri – Center of Excellence for Advanced Materials Research (CEAMR), King Abdulaziz University, 21589 Jeddah, Saudi Arabia; [orcid.org/0000-0001-7905-3209](https://orcid.org/0000-0001-7905-3209)

Mohammad Khaja Nazeeruddin – Group for Molecular Engineering of Functional Materials, Institute of Chemical Sciences and Engineering, École Polytechnique Fédérale de Lausanne, Lausanne CH-1015, Switzerland; [orcid.org/0000-0001-5955-4786](https://orcid.org/0000-0001-5955-4786)

Gianluca Pozzi – Institute of Chemical Sciences and Technologies “Giulio Natta” of National Research Council, I-20133 Milano, Italy; [orcid.org/0000-0002-1469-9284](https://orcid.org/0000-0002-1469-9284)

Complete contact information is available at:  
<https://pubs.acs.org/10.1021/acs.jpcc.2c06152>

## Notes

The authors declare no competing financial interest.

## ACKNOWLEDGMENTS

P.G. and S.O. acknowledge the financial support from the NSFC-CNR exchange program (NSFC Grant No. 22011530391) and the National Natural Science Foundation of China (Grant No. 21975260). The authors are grateful to Prof. A. Vertova and Prof. A. Minguzzi (University of Milan) for Cyclic Voltammetry measurements. M.S. thanks the German Research Foundation (DFG) for funding (SPP2196, 431314977/GRK 2642). M.S. acknowledges funding by ProperPhotoMile. Project ProperPhotoMile is supported under the umbrella of SOLAR-ERA.NET Cofund 2 by the Spanish Ministry of Science and Education and the AEI under the project PCI2020-112185 and CDTI project number IDI-20210171; the Federal Ministry for Economic Affairs and Energy on the basis of a decision by the German Bundestag project number FKZ 03EE1070B and FKZ 03EE1070A and the Israel Ministry of Energy with project number 220-11-031. SOLAR-ERA.NET is supported by the European Commission within the EU Framework Programme for Research and Innovation HORIZON 2020 (Cofund ERA-NET Action, No. 786483).

## REFERENCES

- (1) Gangala, S.; Misra, R. Spiro-Linked Organic Small Molecules as Hole-Transport Materials for Perovskite Solar Cells. *J. Mater. Chem. A* **2018**, *6*, 18750–18765.
- (2) Burschka, J.; Pellet, N.; Moon, S. J.; Humphry-Baker, R.; Gao, P.; Nazeeruddin, M. K.; Grätzel, M. Sequential Deposition as a Route to High-Performance Perovskite-Sensitized Solar Cells. *Nature* **2013**, *499*, 316–319.
- (3) Ma, S.; Zhang, H.; Zhao, N.; Cheng, Y.; Wang, M.; Shen, Y.; Tu, G. Spiro-Thiophene Derivatives as Hole-Transport Materials for Perovskite Solar Cells. *J. Mater. Chem. A* **2015**, *3*, 12139–12144.
- (4) Deng, Z.; He, M.; Zhang, Y.; Ullah, F.; Ding, K.; Liang, J.; Zhang, Z.; Xu, H.; Qiu, Y.; Xie, Z.; et al. Design of Low Crystallinity Spiro-Typed Hole Transporting Material for Planar Perovskite Solar Cells to Achieve 21.76% Efficiency. *Chem. Mater.* **2021**, *33*, 285–297.
- (5) Green, M. A.; Ho-Baillie, A.; Snaith, H. J. The Emergence of Perovskite Solar Cells. *Nat. Photonics* **2014**, *8*, 506–514.
- (6) Zhou, Q.; Gao, Y.; Cai, C.; Zhang, Z.; Xu, J.; Yuan, Z.; Gao, P. Dually-Passivated Perovskite Solar Cells with Reduced Voltage Loss and Increased Super Oxide Resistance. *Angew. Chem., Int. Ed.* **2021**, *60*, 8303–8312.
- (7) Xu, B.; Bi, D.; Hua, Y.; Liu, P.; Cheng, M.; Grätzel, M.; Kloo, L.; Hagfeldt, A.; Sun, L. A Low-Cost Spiro[Fluorene-9,9'-Xanthene]-Based Hole Transport Material for Highly Efficient Solid-State Dye-Sensitized Solar Cells and Perovskite Solar Cells. *Energy Environ. Sci.* **2016**, *9*, 873–877.
- (8) Wang, Y.; Zhu, Z.; Chueh, C.-C.; Jen, A. K.-Y.; Chi, Y. Spiro-Phenylpyrazole-9,9'-Thioxanthene Analogues as Hole-Transporting Materials for Efficient Planar Perovskite Solar Cells. *Adv. Energy Mater.* **2017**, *7*, No. 1700823.
- (9) Jeong, M.; Choi, I. W.; Go, E. M.; Cho, Y.; Kim, M.; Lee, B.; Jeong, S.; Jo, Y.; Choi, H. W.; Lee, J.; et al. Stable Perovskite Solar Cells with Efficiency Exceeding 24.8% and 0.3-V Voltage Loss. *Science* **2020**, *369*, 1615–1620.
- (10) Dong, Q.; Fang, Y.; Shao, Y.; Mulligan, P.; Qiu, J.; Cao, L.; Huang, J. Electron-Hole Diffusion Lengths > 175 m m in Solution-Grown CH<sub>3</sub>NH<sub>3</sub>PbI<sub>3</sub> Single Crystals. *Science* **2015**, *347*, 967–970.
- (11) Stranks, S. D.; Eperon, G. E.; Grancini, G.; Menelaou, C.; Alcocer, M. J. P.; Leijtens, T.; Herz, L. M.; Petrozza, A.; Snaith, H. J. Electron-Hole Diffusion Lengths Exceeding 1 Micrometer in an Organometal Trihalide Perovskite Absorber. *Science* **2013**, *342*, 341–344.
- (12) Xing, G.; Mathews, N.; Sun, S.; Lim, S. S.; Lam, Y. M.; Grätzel, M.; Mhaisalkar, S.; Sum, T. C. Long-Range Balanced Electron- and Hole-Transport Lengths in Organic-Inorganic CH<sub>3</sub>NH<sub>3</sub>PbI<sub>3</sub>. *Science* **2013**, *342*, 344–347.
- (13) Xu, J.; Liang, L.; Mai, C.; Zhang, Z.; Zhou, Q.; Xiong, Q.; Zhang, Z.; Deng, L.; Gao, P. Lewis-Base Containing Spiro Type Hole Transporting Materials for High-Performance Perovskite Solar Cells with Efficiency Approaching 20%. *Nanoscale* **2020**, *12*, 13157–13164.
- (14) Gao, P.; Grätzel, M.; Nazeeruddin, M. K. Organohalide Lead Perovskites for Photovoltaic Applications. *Energy Environ. Sci.* **2014**, *7*, 2448–2463.
- (15) Sallenave, X.; Shasti, M.; Anaraki, E. H.; Volyniuk, D.; Grazulevicius, J. V.; Zakeeruddin, S. M.; Mortezaali, A.; Grätzel, M.; Hagfeldt, A.; Sini, G. Interfacial and Bulk Properties of Hole Transporting Materials in Perovskite Solar Cells: Spiro-MeTAD versus Spiro-OMeTAD. *J. Mater. Chem. A* **2020**, *8*, 8527–8539.
- (16) Zhang, Z.; Gao, Y.; Li, Z.; Qiao, L.; Xiong, Q.; Deng, L.; Zhang, Z.; Long, R.; Zhou, Q.; Du, Y.; et al. Marked Passivation Effect of Naphthalene-1,8-Dicarboximides in High-Performance Perovskite Solar Cells. *Adv. Mater.* **2021**, *33*, No. 2008405.
- (17) Liang, L.; Luo, H.; Hu, J.; Li, H.; Gao, P. Efficient Perovskite Solar Cells by Reducing Interface-Mediated Recombination: A Bulky Amine Approach. *Adv. Energy Mater.* **2020**, *10*, No. 2000197.
- (18) Saragi, T. P. I.; Spehr, T.; Siebert, A.; Fuhrmann-Lieker, T.; Salbeck, J. Spiro Compounds for Organic Optoelectronics. *Chem. Rev.* **2007**, *107*, 1011–1065.

- (19) Jeux, V.; Dalinot, C.; Allain, M.; Sanguinet, L.; Leriche, P. Synthesis of Spiro[Cyclopenta[1,2-b:5,4-b']DiThiophene-4,9'-Fluorenes] SDTF Dissymmetrically Functionalized. *Tetrahedron Lett.* **2015**, *56*, 1383–1387.
- (20) Kojima, A.; Teshima, K.; Shirai, Y.; Miyasaka, T. Organometal Halide Perovskites as Visible-Light Sensitizers for Photovoltaic Cells. *J. Am. Chem. Soc.* **2009**, *131*, 6050–6051.
- (21) National Renewable Energy Laboratory (NREL) Best Research-Cell Efficiency, 2022. <https://www.nrel.gov/pv/cell-efficiency.html/>. (accessed October 8, 2022).
- (22) Yang, W. S.; Park, B. W.; Jung, E. H.; Jeon, N. J.; Kim, Y. C.; Lee, D. U.; Shin, S. S.; Seo, J.; Kim, E. K.; Noh, J. H.; Seok, S. I. Iodide Management in Formamidinium-Lead-Halide-Based Perovskite Layers for Efficient Solar Cells. *Science* **2017**, *356*, 1376–1379.
- (23) Kim, H. S.; Lee, C. R.; Im, J. H.; Lee, K. B.; Moehl, T.; Marchioro, A.; Moon, S. J.; Humphry-Baker, R.; Yum, J. H.; Moser, J. E.; et al. Lead Iodide Perovskite Sensitized All-Solid-State Submicron Thin Film Mesoscopic Solar Cell with Efficiency Exceeding 9%. *Sci. Rep.* **2012**, *2*, No. 591.
- (24) Yang, W. S.; Noh, J. H.; Jeon, N. J.; Kim, Y. C.; Ryu, S.; Seo, J.; Seok, S. I. High-Performance Photovoltaic Perovskite Layers Fabricated through Intramolecular Exchange. *Science* **2015**, *348*, 1234–1237.
- (25) Jiang, Q.; Zhao, Y.; Zhang, X.; Yang, X.; Chen, Y.; Chu, Z.; Ye, Q.; Li, X.; Yin, Z.; You, J. Surface Passivation of Perovskite Film for Efficient Solar Cells. *Nat. Photonics* **2019**, *13*, 460–466.
- (26) Nakar, R.; Ramos, F. J.; Dalinot, C.; Marques, P. S.; Cabanetos, C.; Leriche, P.; Sanguinet, L.; Kobeissi, M.; Blanchard, P.; Faure-Vincent, J.; et al. Cyclopentadithiophene and Fluorene Spiro-Core-Based Hole-Transporting Materials for Perovskite Solar Cells. *J. Phys. Chem. C* **2019**, *123*, 22767–22774.
- (27) Saliba, M.; Orlandi, S.; Matsui, T.; Aghazada, S.; Cavazzini, M.; Correa-Baena, J.-P.; Gao, P.; Scopelliti, R.; Mosconi, E.; Dahmen, K.-H.; et al. A Molecularly Engineered Hole-Transporting Material for Efficient Perovskite Solar Cells. *Nat. Energy* **2016**, *1*, No. 15017.
- (28) Franckevičius, M.; Mishra, A.; Kreuzer, F.; Luo, J.; Zakeeruddin, S. M.; Grätzel, M. A Dopant-Free Spirobi[Cyclopenta[2,1-b:3,4-b']Dithiophene] Based Hole-Transport Material for Efficient Perovskite Solar Cells. *Mater. Horiz.* **2015**, *2*, 613–618.
- (29) Lin, J. H.; Elangovan, A.; Ho, T. I. Structure-Property Relationships in Conjugated Donor-Acceptor Molecules Based on Cyanoanthracene: Computational and Experimental Studies. *J. Org. Chem.* **2005**, *70*, 7397–7407.
- (30) Pozzi, G.; Orlandi, S.; Cavazzini, M.; Minudri, D.; Macor, L.; Otero, L.; Fungo, F.; Molecolari, T. Synthesis and Photovoltaic Applications of a 4,4'-Spirobi[cyclopenta-[2,1-b;3,4-b']dithiophene]-Bridged Donor/Acceptor Dye. *Org. Lett.* **2013**, *15*, 4642–4645.
- (31) Frisch, M. J.; Trucks, G. W.; Schlegel, H. B.; Scuseria, G. E.; Robb, M. A.; Cheeseman, J. R.; Scalmani, G.; Barone, V.; Mennucci, B.; Petersson, G. A. et al. *Gaussian 09*, Revision A.1; Gaussian, Inc.: Wallingford, CT, 2009.
- (32) Lu, T.; Chen, F. Multiwfn: A Multifunctional Wavefunction Analyzer. *J. Comput. Chem.* **2012**, *33*, 580–592.
- (33) Rakstys, K.; Saliba, M.; Gao, P.; Gratia, P.; Kamaraukas, E.; Paek, S.; Jankauskas, V.; Nazeeruddin, M. K. Highly Efficient Perovskite Solar Cells Employing an Easily Attainable Bifluorenylidene-Based Hole-Transporting Material. *Angew. Chem., Int. Ed.* **2016**, *55*, 7464–7468.
- (34) Ren, M.; Wang, J.; Xie, X.; Zhang, J.; Wang, P. Double-Helicene-Based Hole-Transporter for Perovskite Solar Cells with 22% Efficiency and Operation Durability. *ACS Energy Lett.* **2019**, *4*, 2683–2688.
- (35) SantosMiranda, M. E.; Marcolla, C.; Rodriguez, C. A.; Wilhelm, H. M.; Sierakowski, M. R.; BelleBresolin, T. M.; de Freitas, R. A. Polymer Electronic Materials: A Review of Charge Transport. *Polym. Int.* **2006**, *55*, 961–969.
- (36) Berlin, A.; Zotti, G.; Zecchin, S.; Schiavon, G.; Vercelli, B.; Zanelli, A. New Low-Gap Polymers from 3,4-Ethylenedioxythiophene-Bis-Substituted Electron-Poor Thiophenes. The Roles of Thiophene, Donor-Acceptor Alternation, and Copolymerization in Intrinsic Conductivity. *Chem. Mater.* **2004**, *16*, 3667–3676.
- (37) Roncali, J. Synthetic Principles for Bandgap Control in Linear  $\pi$ -Conjugated Systems. *Chem. Rev.* **1997**, *97*, 173–205.
- (38) Cardona, C. M.; Li, W.; Kaifer, A. E.; Stockdale, D.; Bazan, G. C. Electrochemical Considerations for Determining Absolute Frontier Orbital Energy Levels of Conjugated Polymers for Solar Cell Applications. *Adv. Mater.* **2011**, *23*, 2367–2371.
- (39) Sun, Z. Z.; Feng, S.; Ding, W. L.; Peng, X. L.; Liu, J. L.; Xu, X. L. Azatriphenylene-Based D-A-D-Typed Hole-Transporting Materials for Perovskite Solar Cells with Tunable Energy Levels and High Mobility. *Sol. Energy* **2021**, *224*, 491–499.
- (40) Hu, W.; Zhang, Z.; Cui, J.; Shen, W.; Li, M.; He, R. Influence of  $\pi$ -Bridge Conjugation on the Electrochemical Properties within Hole Transporting Materials for Perovskite Solar Cells. *Nanoscale* **2017**, *9*, 12916–12924.
- (41) Duan, Y. A.; Geng, Y.; Li, H.-B.; Jin, J. L.; Wu, Y.; Su, Z.-M. Theoretical Characterization and Design of Small Molecule Donor Material Containing Naphthodithiophene Central Unit for Efficient Organic Solar Cells. *J. Comput. Chem.* **2013**, *34*, 1611–1619.
- (42) Scholes, G. D.; Rumbles, G. Excitons in Nanoscale Systems. In *Materials for Sustainable Energy*; World Scientific, 2010; Vol. 5, pp 12–25.
- (43) Zhang, Z. L.; Zou, L. Y.; Ren, A. M.; Liu, Y. F.; Feng, J. K.; Sun, C. C. Theoretical Studies on the Electronic Structures and Optical Properties of Star-Shaped Triazatruxene/Heterofluorene Co-Polymers. *Dyes Pigm.* **2013**, *96*, 349–363.
- (44) Cao, C.; Chen, Y.-w.; Wu, Y.; Deumens, E.; Cheng, H.-P. OPAL: A Multiscale Multicenter Simulation Package Based on MPI-2 Protocol. *Int. J. Quantum Chem.* **2011**, *111*, 4020–4029.
- (45) Shi, D.; Qin, X.; Li, Y.; He, Y.; Zhong, C.; Pan, J.; Dong, H.; Xu, W.; Li, T.; Hu, W.; et al. Spiro-OMeTAD Single Crystals: Remarkably Enhanced Charge-Carrier Transport via Mesoscale Ordering. *Sci. Adv.* **2016**, *2*, No. e1501491.
- (46) Bader, R. F. W. A Quantum Theory of Molecular Structure and Its Applications. *Chem. Rev.* **1991**, *91*, 893–928.
- (47) Fang, L.; Zheng, A.; Ren, M.; Xie, X.; Wang, P. Unraveling the Structure-Property Relationship of Molecular Hole-Transporting Materials for Perovskite Solar Cells. *ACS Appl. Mater. Interfaces* **2019**, *11*, 39001–39009.
- (48) Xu, N.; Zheng, A.; Wei, Y.; Yuan, Y.; Zhang, J.; Lei, M.; Wang, P. D- $\pi$ -D Molecular Semiconductors for Perovskite Solar Cells: The Superior Role of Helical versus Planar  $\pi$ -Linkers. *Chem. Sci.* **2020**, *11*, 3418–3426.
- (49) Xu, N.; Li, Y.; Ricciarelli, D.; Wang, J.; Mosconi, E.; Yuan, Y.; De Angelis, F.; Zakeeruddin, S. M.; Grätzel, M.; Wang, P. An Oxa[5]Helicene-Based Racemic Semiconducting Glassy Film for Photothermally Stable Perovskite Solar Cells. *iScience* **2019**, *15*, 234–242.
- (50) Wang, J.; Shi, H.; Xu, N.; Zhang, J.; Yuan, Y.; Lei, M.; Wang, L.; Wang, P. Aza[5]Helicene Rivals N-Annulated Perylene as  $\pi$ -Linker of D- $\pi$ -D Typed Hole-Transporters for Perovskite Solar Cells. *Adv. Funct. Mater.* **2020**, *30*, No. 2002114.
- (51) Zheng, A.; Xie, X.; Wang, Y.; Xu, N.; Zhang, J.; Yuan, Y.; Wang, P. A Triple Axial Chirality, Racemic Molecular Semiconductor Based on Thiahelicene and Ethylenedioxythiophene for Perovskite Solar Cells: Microscopic Insights on Performance Enhancement. *Adv. Funct. Mater.* **2021**, *31*, No. 2009854.
- (52) Bayly, C. I.; Merz, K. M.; Ferguson, D. M.; Cornell, W. D.; Fox, T.; Caldwell, J. W.; Kollman, P. A.; Cieplak, P.; Gould, I. R.; Spellmeyer, D. C. A Second Generation Force Field for the Simulation of Proteins, Nucleic Acids, and Organic Molecules. *J. Am. Chem. Soc.* **1995**, *117*, 5179–5197.
- (53) Hutchison, G. R.; Ratner, M. A.; Marks, T. J. Hopping Transport in Conductive Heterocyclic Oligomers: Reorganization Energies and Substituent Effects. *J. Am. Chem. Soc.* **2005**, *127*, 2339–2350.

(54) Nelsen, S. F.; Trieber, D. A.; Ismagilov, R. F.; Teki, Y. Solvent Effects on Charge Transfer Bands of Nitrogen-Centered Intervalence Compounds. *J. Am. Chem. Soc.* **2001**, *123*, 5684–5694.

(55) Marcus, R. A. Electron Transfer Reactions in Chemistry: Theory and Experiment (Nobel Lecture). *Angew. Chem., Int. Ed.* **1993**, *32*, 1111–1121.

(56) Yavuz, I.; Martin, B. N.; Park, J.; Houk, K. N. Theoretical Study of the Molecular Ordering, Paracrystallinity, and Charge Mobilities of Oligomers in Different Crystalline Phases. *J. Am. Chem. Soc.* **2015**, *137*, 2856–2866.

(57) Chen, W.; Wang, Y.; Liu, B.; Gao, Y.; Wu, Z.; Shi, Y.; Tang, Y.; Yang, K.; Zhang, Y.; Sun, W.; et al. Engineering of Dendritic Dopant-Free Hole Transport Molecules: Enabling Ultrahigh Fill Factor in Perovskite Solar Cells with Optimized Dendron Construction. *Sci. China Chem.* **2021**, *64*, 41–51.

(58) Daskeviciute, S.; Momblona, C.; Rakstys, K.; Sutanto, A. A.; Daskeviciene, M.; Jankauskas, V.; Gruodis, A.; Bubniene, G.; Getautis, V.; Nazeeruddin, M. K. Fluorene-Based Enamines as Low-Cost and Dopant-Free Hole Transporting Materials for High Performance and Stable Perovskite Solar Cells. *J. Mater. Chem. A* **2021**, *9*, 301–309.

(59) Vasilopoulou, M.; Fakharuddin, A.; Coutsolelos, A. G.; Falaras, P.; Argitis, P.; Yusoff, A. R. B. M.; Nazeeruddin, M. K. Molecular Materials as Interfacial Layers and Additives in Perovskite Solar Cells. *Chem. Soc. Rev.* **2020**, *49*, 4496–4526.

(60) Zhou, W.; Wen, Z.; Gao, P. Less Is More: Dopant-Free Hole Transporting Materials for High-Efficiency Perovskite Solar Cells. *Adv. Energy Mater.* **2018**, *8*, No. 1702512.

(61) Zhang, Z.; Liang, L.; Deng, L.; Ren, L.; Zhao, N.; Huang, J.; Yu, Y.; Gao, P. Fused Dithienopicenocarbazole Enabling High Mobility Dopant-Free Hole-Transporting Polymers for Efficient and Stable Perovskite Solar Cells. *ACS Appl. Mater. Interfaces* **2021**, *13*, 6688–6698.

(62) Rakstys, K.; Igci, C.; Nazeeruddin, M. K. Efficiency: Vs. Stability: Dopant-Free Hole Transporting Materials towards Stabilized Perovskite Solar Cells. *Chem. Sci.* **2019**, *10*, 6748–6769.

(63) Wang, Y.; Chen, W.; Wang, L.; Tu, B.; Chen, T.; Liu, B.; Yang, K.; Koh, C. W.; Zhang, X.; Sun, H.; et al. Dopant-Free Small-Molecule Hole-Transporting Material for Inverted Perovskite Solar Cells with Efficiency Exceeding 21%. *Adv. Mater.* **2019**, *31*, No. 1902781.

(64) Sun, X.; Wu, F.; Zhong, C.; Zhu, L.; Li, Z. A Structure-Property Study of Fluoranthene-Cored Hole-Transporting Materials Enables 19.3% Efficiency in Dopant-Free Perovskite Solar Cells. *Chem. Sci.* **2019**, *10*, 6899–6907.

(65) Sutanto, A. A.; Joseph, V.; Igci, C.; Syzgantseva, O. A.; Syzgantseva, M. A.; Jankauskas, V.; Rakstys, K.; Queloz, V. I. E.; Huang, P. Y.; Ni, J. S.; et al. Isomeric Carbazole-Based Hole-Transporting Materials: Role of the Linkage Position on the Photovoltaic Performance of Perovskite Solar Cells. *Chem. Mater.* **2021**, *33*, 3286–3296.

(66) Wang, Y.; Yue, Y.; Yang, X.; Han, L. Toward Long-Term Stable and Highly Efficient Perovskite Solar Cells via Effective Charge Transporting Materials. *Adv. Energy Mater.* **2018**, *8*, No. 1800249.

(67) Zhang, J.; Xu, B.; Johansson, M. B.; Vlachopoulos, N.; Boschloo, G.; Sun, L.; Johansson, E. M. J.; Hagfeldt, A. Strategy to Boost the Efficiency of Mixed-Ion Perovskite Solar Cells: Changing Geometry of the Hole Transporting Material. *ACS Nano* **2016**, *10*, 6816–6825.

(68) Chi, W. J.; Li, Q. S.; Li, Z. S. Effects of Molecular Configuration on Charge Diffusion Kinetics within Hole-Transporting Materials for Perovskites Solar Cells. *J. Phys. Chem. C* **2015**, *119*, 8284–8590.

(69) Calió, L.; Kazim, S.; Grätzel, M.; Ahmad, S. Hole-Transport Materials for Perovskite Solar Cells. *Angew. Chem., Int. Ed.* **2016**, *55*, 14522–14545.

(70) Torres, A.; Rego, L. G. C. Surface Effects and Adsorption of Methoxy Anchors on Hybrid Lead Iodide Perovskites: Insights for Spiro-MeOTAD Attachment. *J. Phys. Chem. C* **2014**, *118*, 26947–26954.

(71) Xu, B.; Zhu, Z.; Zhang, J.; Liu, H.; Chueh, C. C.; Li, X.; Jen, A. K. Y. 4-Tert-Butylpyridine Free Organic Hole Transporting Materials for Stable and Efficient Planar Perovskite Solar Cells. *Adv. Energy Mater.* **2017**, *7*, No. 1700683.

## Recommended by ACS

### Less Is More: Simplified Fluorene-Based Dopant-Free Hole Transport Materials Promote the Long-Term Ambient Stability of Perovskite Solar Cells

Paavo Mäkinen, Paola Vivo, et al.

MARCH 14, 2023

CHEMISTRY OF MATERIALS

READ 

### Exploration of the Effect of Fluoridation on the Doping-Free Linear Dibenzothiophene-Based Hole-Transport Material Applied for Inverted Perovskite Solar Cells

Zhengxu Liu, Ningyi Yuan, et al.

JANUARY 25, 2023

ACS APPLIED ENERGY MATERIALS

READ 

### Constructing Efficient Hole Transport Material through $\pi$ -Conjunction Extension for Perovskite Solar Cell

Haoxin Wang, Ming Cheng, et al.

OCTOBER 18, 2022

ACS APPLIED ENERGY MATERIALS

READ 

### Modification on the Quinoxaline Unit to Achieve High Open-Circuit Voltage and Morphology Optimization for Organic Solar Cells

Zhenyu Chen, Ziyi Ge, et al.

SEPTEMBER 15, 2022

ACS ENERGY LETTERS

READ 

Get More Suggestions >